FERMILAB-PUB-20-288-AD-ND

Updated MiniBooNE neutrino oscillation results with increased data and new background studies

A. A. Aguilar-Arevalo[14], B. C. Brown[5], J. M. Conrad[13], R. Dharmapalan[1,7], A. Diaz[13], Z. Djurcic[2], D. A. Finley[5], R. Ford[5], G. T. Garvey[10], S. Gollapinni[10], A. Hourlier[13], E.-C. Huang[10], N. W. Kamp[13], G. Karagiorgi[4], T. Katori[12], T. Kobilarcik[5], K. Lin[4,10], W. C. Louis[10], C. Mariani[17], W. Marsh[5], G. B. Mills[10,†], J. Mirabal-Martinez[10], C. D. Moore[5], R. H. Nelson[3,⋆], J. Nowak[9], I. Parmaksiz[16], Z. Pavlovic[5], H. Ray[6], B. P. Roe[15], A. D. Russell[5], A. Schneider[13], M. H. Shaevitz[4], H. Siegel[4], J. Spitz[15], I. Stancu[1], R. Tayloe[8], R. T. Thornton[10], M. Tzanov[3,11], R. G. Van de Water[10], D. H. White[10,†], E. D. Zimmerman[3]

(The MiniBooNE Collaboration)

[1] *University of Alabama; Tuscaloosa, AL 35487, USA*

[2] *Argonne National Laboratory; Argonne, IL 60439, USA*

[3] *University of Colorado; Boulder, CO 80309, USA*

[4] *Columbia University; New York, NY 10027, USA*

[5] *Fermi National Accelerator Laboratory; Batavia, IL 60510, USA*

[6] *University of Florida; Gainesville, FL 32611, USA*

[7] *University of Hawaii, Manoa; Honolulu, HI 96822, USA*

[8] *Indiana University; Bloomington, IN 47405, USA*

[9] *Lancaster University; Lancaster LA1 4YB, UK*

[10] *Los Alamos National Laboratory; Los Alamos,*

This document was prepared by MiniBooNE collaboration using the resources of the Fermi National Accelerator Laboratory (Fermilab), a U.S. Department of Energy, Office of Science, HEP User Facility. Fermilab is managed by Fermi Research Alliance, LLC (FRA), acting under Contract No. DE-AC02-07CH11359.

NM 87545, USA

[11]*Louisiana State University; Baton Rouge,*

LA 70803, USA

[12]*King's College London; London WC2R 2LS, UK*

[13]*Massachusetts Institute of Technology; Cambridge,*

MA 02139, USA

[14]*Instituto de Ciencias Nucleares; Universidad*

Nacional Autónoma de México; CDMX 04510, México

[15]*University of Michigan; Ann Arbor,*

MI 48109, USA

[16]*University of Texas at Arlington,*

Arlington, TX 76019

[17]*Center for Neutrino Physics; Virginia Tech; Blacksburg,*

VA 24061, USA

[⋆]*Now at The Aerospace Corporation,*

Los Angeles, CA 90009, USA

[†]*Deceased*

(Dated: March 3, 2021)

Abstract

The MiniBooNE experiment at Fermilab reports a total excess of $638.0 \pm 52.1(stat.) \pm 122.2(syst.)$ electronlike events from a data sample corresponding to 18.75×10^{20} protons-on-target in neutrino mode, which is a 46% increase in the data sample with respect to previously published results, and 11.27×10^{20} protons-on-target in antineutrino mode. The overall significance of the excess, 4.8σ, is limited by systematic uncertainties, assumed to be Gaussian, as the statistical significance of the excess is 12.2σ. The additional statistics allow several studies to address questions on the source of the excess. First, we provide two-dimensional plots in visible energy and cosine of the angle of the outgoing lepton, which can provide valuable input to models for the event excess. Second, we test whether the excess may arise from photons that enter the detector from external events or photons exiting the detector from π^0 decays in two model independent ways. Beam timing information shows that almost all of the excess is in time with neutrinos that interact in the detector. The radius distribution shows that the excess is distributed throughout the volume, while tighter cuts on the fiducial volume increase the significance of the excess. The data likelihood ratio disfavors models that explain the event excess due to entering or exiting photons.

I. INTRODUCTION

The LSND [1] and MiniBooNE [2, 3] experiments have reported excesses of ν_e and $\bar{\nu}_e$ charge-current quasielastic (CCQE) events in ν_μ beams. Exotic models beyond the three-neutrino paradigm that have been invoked to explain these anomalies include, for example, 3+N neutrino oscillation models involving three active neutrinos and N additional sterile neutrinos [4–14], resonant neutrino oscillations [15], Lorentz violation [16], sterile neutrino decay [17], scalar decay [18], sterile neutrino nonstandard interactions [19], and altered dispersion relations with sterile neutrinos [20]. This paper presents improved MiniBooNE ν_e appearance results with increased statistics and with additional studies that disfavor neutral-current (NC) π^0 and external event backgrounds.

II. THE MINIBOONE EXPERIMENT

The MiniBooNE experiment makes use of the Booster Neutrino Beam (BNB) that is produced by 8 GeV protons from the Fermilab Booster interacting on a beryllium target inside a magnetic focusing horn, followed by meson decay in a 50 m decay pipe. In neutrino mode, the ν_μ, $\bar{\nu}_\mu$, ν_e, and $\bar{\nu}_e$ flux contributions at the detector are 93.5%, 5.9%, 0.5%, and 0.1%, respectively, while in antineutrino mode, the flux contributions are 15.7%, 83.7%, 0.2%, and 0.4%, respectively. The ν_μ and $\bar{\nu}_\mu$ fluxes peak at approximately 600 MeV and 400 MeV, respectively. The MiniBooNE detector, described in detail in reference [21], consists of a 12.2 m diameter sphere filled with 818 tonnes of pure mineral oil (CH_2) and is located 541 m from the beryllium target. The detector is covered by 1520 8-inch photomultiplier tubes (PMTs), where 1280 PMTs are in the interior detector region and 240 PMTs are located in the optically isolated outer veto region. The PMTs detect the directed Cherenkov light and the isotropic scintillation light produced by charged particles from neutrino interactions in the mineral oil. Events are reconstructed [22] from the hit PMT charge and time information, and the reconstructed neutrino energy, E_ν^{QE}, is estimated from the measured energy and angle of the outgoing muon or electron, assuming the kinematics of CCQE scattering [23]. The MiniBooNE experiment has collected data from 2002-2019, based on a total of 11.27×10^{20} protons-on-target (POT) in antineutrino mode and 18.75×10^{20} POT in neutrino mode. Also, a special beam off-target run collected an additional 1.86×10^{20} POT in a search for sub-

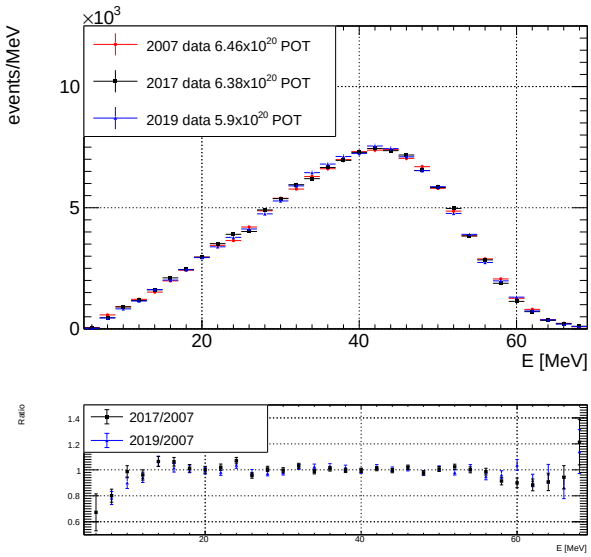

FIG. 1: The Michel electron energy distribution for the first, second, and third running periods in neutrino mode. The events are normalized to the first running period. The bottom plot shows ratios of the second and third running periods to the first running period.

GeV dark matter [24]. During the 17 years of running, the BNB and MiniBooNE detector have been stable to within 3% in neutrino energy. Fig. 1 shows the energy distribution of Michel electrons from stopped muon decay for the first (6.46×10^{20} POT from 2002 to 2007), second (6.38×10^{20} POT from 2015 to 2017), and third running periods (5.91×10^{20} POT from 2017 to 2019) in neutrino mode. By adjusting the energy calibration by 2% for the second running period and by 3% for the third running period, good agreement is obtained for the Michel electron energy distribution.

III. DATA ANALYSIS

The data analysis is optimized to measure ν_e-induced CCQE events and reject ν_μ induced events, and is identical to the previous analysis [2]. Figs. 2, 3, and 4 show the ν_e CCQE data and background for the three particle identification variables in neutrino mode in the $200 < E_\nu^{QE} < 1250$ MeV energy range for the total 18.75×10^{20} POT data. The comparison between data and background for the full range of particle identification variables was shown in the supplementary material of a previous publication [3]. The average selection efficiency is $\sim 20\%$ ($\sim 0.1\%$) for ν_e-induced CCQE events (ν_μ-induced background events)

generated over the fiducial volume. The fraction of CCQE events in antineutrino mode that are from wrong-sign neutrino events was determined from the angular distributions of muons created in CCQE interactions and by measuring CC single π^+ events [25]. Table I shows the predicted but unconstrained ν_e and $\bar{\nu}_e$ CCQE background events for the neutrino energy range $200 < E_\nu^{QE} < 1250$ MeV for both neutrino and antineutrino modes, where there are approximately twice as many Monte Carlo events compared to data events. Table I also shows the total constrained background, where the overall normalization of the ν_e intrinsic background is constrained by the ν_μ CCQE event sample. The upper limit of 1250 MeV was chosen by the collaboration before unblinding the data in 2007, while the lower limit of 200 MeV was chosen in 2013 [2] because it is the lowest energy for reliably reconstructing the Cherenkov ring of ν_μ CCQE events with a visible energy greater than 140 MeV. From the given detector resolution estimated from the Michel electron spectrum (Fig. 1), there is a negligible amount of migration from events below 200 MeV. Note that the original lower limit was chosen to be 300 MeV before unblinding the data in 2007. During the unblinding procedure, the lower limit was increased to 475 MeV due to the low probability of the two-neutrino oscillation fit and worries about the single-gamma background. However, careful studies of the single-gamma background were performed after unblinding and convinced the collaboration that the single-gamma background was estimated correctly within systematic uncertainties and agreed with theoretical calculations [31]. Finally, Table I shows the expected number of events corresponding to the LSND best fit oscillation probability of 0.26%, assuming large Δm^2 where the oscillations are washed out. LSND and MiniBooNE have the same average value of L/E, but MiniBooNE has a larger range of L/E. Therefore, the appearance probabilities for LSND and MiniBooNE should not be exactly the same at lower L/E values. Figs. 5 and 6 show the ν_μ CCQE E_ν^{QE} energy distribution and the NC π^0 mass distribution in neutrino mode for the first, second, and third running periods. As shown in the figures, the three running periods have good agreement.

Systematic uncertainties are determined by considering the predicted effects on the ν_μ, $\bar{\nu}_\mu$, ν_e, and $\bar{\nu}_e$ CCQE rates from variations of model parameters that include uncertainties in the neutrino and antineutrino flux estimates, uncertainties in neutrino cross sections, uncertainties from nuclear effects, and uncertainties in detector modeling and reconstruction. A covariance matrix in bins of E_ν^{QE} is constructed by considering the variation from each

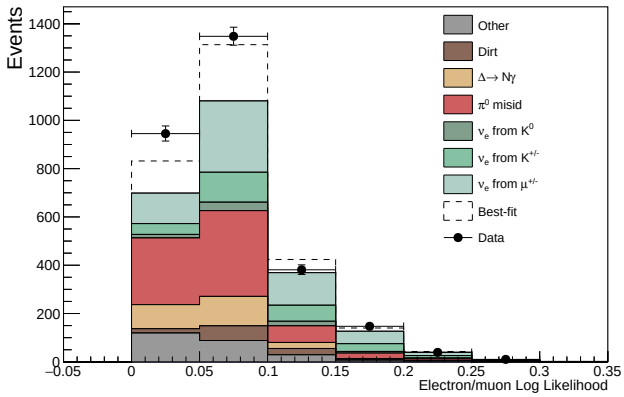

FIG. 2: The MiniBooNE neutrino mode electron-muon particle identification distributions, corresponding to the total 18.75×10^{20} POT data in the $200 < E_\nu^{QE} < 1250$ MeV energy range, for ν_e CCQE data (points with statistical errors) and background (colored histogram). The dashed histogram shows the best fit to the neutrino-mode data assuming two-neutrino oscillations.

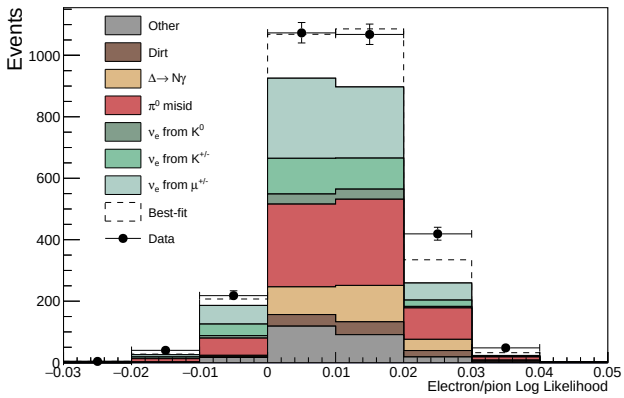

FIG. 3: The MiniBooNE neutrino mode electron-pion particle identification distributions, corresponding to the total 18.75×10^{20} POT data in the $200 < E_\nu^{QE} < 1250$ MeV energy range, for ν_e CCQE data (points with statistical errors) and background (colored histogram). The dashed histogram shows the best fit to the neutrino-mode data assuming two-neutrino oscillations.

source of systematic uncertainty on the ν_e and $\bar{\nu}_e$ CCQE signal and background, and the ν_μ and $\bar{\nu}_\mu$ CCQE prediction as a function of E_ν^{QE}. This matrix includes correlations between any of the ν_e and $\bar{\nu}_e$ CCQE signal and background and ν_μ and $\bar{\nu}_\mu$ CCQE samples, and is used in the χ^2 calculation of the oscillation fits.

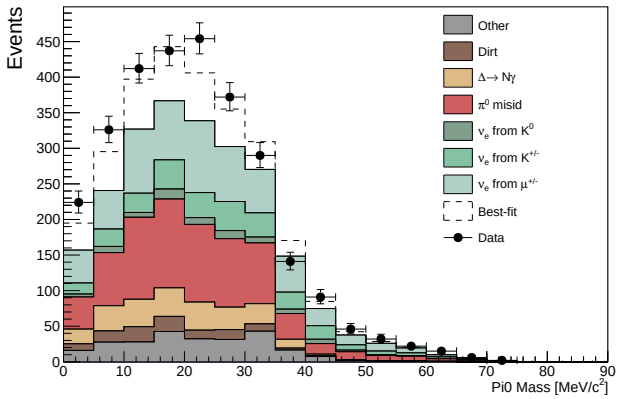

FIG. 4: The MiniBooNE neutrino mode two-ring invariant-mass particle identification distributions, corresponding to the total 18.75×10^{20} POT data in the $200 < E_\nu^{QE} < 1250$ MeV energy range, for ν_e CCQE data (points with statistical errors) and background (colored histogram). The dashed histogram shows the best fit to the neutrino-mode data assuming two-neutrino oscillations.

IV. ELECTRON-NEUTRINO APPEARANCE RESULTS

Figs. 7, 8, and 9 show the visible energy, $\cos\theta$, and E_ν^{QE} distributions for ν_e CCQE data and background in neutrino mode in the $200 < E_\nu^{QE} < 1250$ MeV energy range for the total 18.75×10^{20} POT data, where θ is the angle of the reconstructed electron relative to the incident beam direction. Each bin of reconstructed E_ν^{QE} corresponds to a distribution of "true" generated neutrino energies, which can overlap adjacent bins. In neutrino mode, a total of 2870 data events pass the ν_e CCQE event selection requirements with $200 < E_\nu^{QE} < 1250$ MeV, compared to a background expectation of $2309.4 \pm 48.1(stat.) \pm 109.5(syst.)$ events. The excess, as shown in Table II, is then 560.6 ± 119.6 events or a 4.7σ effect. Fig. 10 shows the event excesses as a function of E_ν^{QE} in neutrino mode for the first, second, and third running periods. Combining the MiniBooNE neutrino and antineutrino data [3], there are a total of 3348 events in the $200 < E_\nu^{QE} < 1250$ MeV energy region, compared to a background expectation of $2710.0 \pm 52.1(stat.) \pm 122.2(syst.)$ events. This corresponds to a total ν_e plus $\bar{\nu}_e$ CCQE excess of $638.0 \pm 52.1(stat.) \pm 122.2(syst.)$ events with respect to expectation, where the statistical uncertainty is the square root of the background estimate and the systematic uncertainty includes correlated and uncorrelated systematic parameters. The overall significance of the excess, 4.8σ, is limited by systematic uncertainties, assumed to be

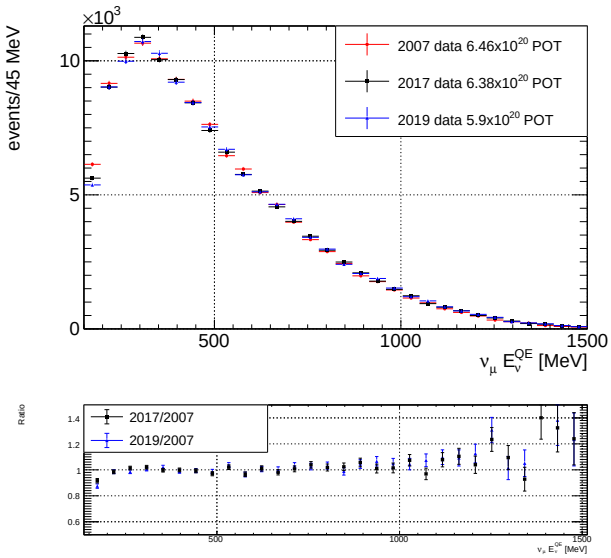

FIG. 5: The ν_μ CCQE muon visible energy distribution for the first, second, and third running periods in neutrino mode. The events are normalized to the first running period. The bottom plot shows ratios of the second and third running periods to the first running period.

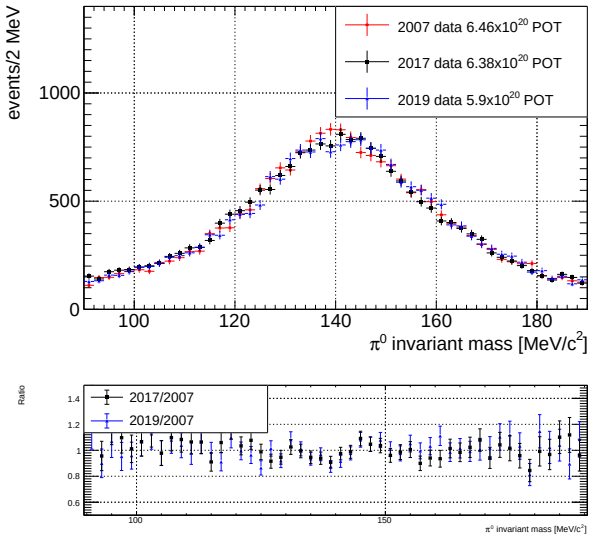

FIG. 6: The NC π^0 mass distribution for the first, second, and third running periods in neutrino mode. The events are normailzed to the first running period. The bottom plot shows ratios of the second and third running periods to the first running period.

TABLE I: *The expected (unconstrained) number of events for the* $200 < E_\nu^{QE} < 1250$ *MeV neutrino energy range from all of the backgrounds in the* ν_e *and* $\bar{\nu}_e$ *appearance analysis before using the constraint from the CC* ν_μ *events. The "Other" backgrounds correspond mostly to neutrino-nucleon and neutrino-electron elastic scattering. Also shown are the constrained background, as well as the expected number of events corresponding to the LSND best fit oscillation probability of 0.26%, assuming oscillations at large* Δm^2*. The table shows the diagonal-element systematic plus statistical uncertainties, which become substantially reduced in the oscillation fits when correlations between energy bins and between the* ν_e *and* ν_μ *events are included.*

Process	Neutrino Mode	Antineutrino Mode
ν_μ & $\bar{\nu}_\mu$ CCQE	107.6 ± 28.2	12.9 ± 4.3
NC π^0	732.3 ± 95.5	112.3 ± 11.5
NC $\Delta \to N\gamma$	251.9 ± 35.2	34.7 ± 5.4
External Events	109.8 ± 15.9	15.3 ± 2.8
Other ν_μ & $\bar{\nu}_\mu$	130.8 ± 33.4	22.3 ± 3.5
ν_e & $\bar{\nu}_e$ from $\mu^\pm$ Decay	621.1 ± 146.3	91.4 ± 27.6
ν_e & $\bar{\nu}_e$ from $K^\pm$ Decay	280.7 ± 61.2	51.2 ± 11.0
ν_e & $\bar{\nu}_e$ from K_L^0 Decay	79.6 ± 29.9	51.4 ± 18.0
Other ν_e & $\bar{\nu}_e$	8.8 ± 4.7	6.7 ± 6.0
Unconstrained Bkgd.	2322.6 ± 258.3	398.2 ± 49.7
Constrained Bkgd.	2309.4 ± 119.6	400.6 ± 28.5
Total Data	2870	478
Excess	560.6 ± 119.6	77.4 ± 28.5
0.26% (LSND) $\nu_\mu \to \nu_e$	676.3	100.0

Gaussian, as the statistical significance of the excess is 12.2σ. The fractional unconstrained systematic uncertainties in the $200 < E_\nu^{QE} < 1250$ MeV energy range are shown in Table III.

In order to test physics models, the numbers of data events, unconstrained background events, and excess events in neutrino mode with visible energy between 150 and 1250 MeV are shown in Figs. 11, 12, and 13 as functions of visible energy and $\cos\theta$. In these figures, there are 20 columns of visible energy from 150 to 1250 MeV and 20 rows of $\cos\theta$ from -1 to

TABLE II: *The number of data events, background events, and excess events in neutrino mode for different selection crteria. The errors include both statistical and systematic uncertainties. Also shown is the significance of each event excess. R is the radius of the reconstructed event interaction point.*

Selection	Data	Background	Excess	Significance
$200 < E_\nu^{QE} < 1250$ MeV & $R < 5m$	2870	2309.4 ± 119.6	560.6 ± 119.6	4.7σ
$150 < E_\nu^{QE} < 1250$ MeV & $R < 5m$	3172	2560.4 ± 131.5	611.6 ± 131.5	4.7σ
$200 < E_\nu^{QE} < 1250$ MeV & $R < 4m$	1978	1519.4 ± 81.9	458.6 ± 81.9	5.6σ
$200 < E_\nu^{QE} < 1250$ MeV & $R < 3m$	864	673.9 ± 41.2	190.1 ± 41.2	4.6σ

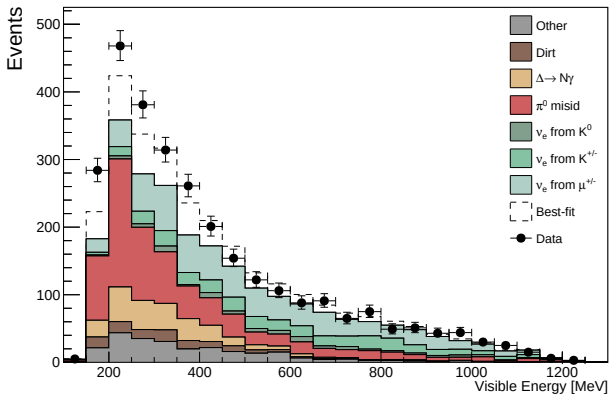

FIG. 7: The MiniBooNE neutrino mode visible energy distributions, corresponding to the total 18.75×10^{20} POT data in the $200 < E_\nu^{QE} < 1250$ MeV energy range, for ν_e CCQE data (points with statistical errors) and background (colored histogram). The dashed histogram shows the best fit to the neutrino-mode data assuming two-neutrino oscillations.

1. There are a total of 3182 data events, 2568.8 background events and 613.2 excess events. Fig. 14 shows the $\cos\theta$ distribution of data and background events for the 20 different energy bins, while Fig. 15 shows the $\cos\theta$ distributions from 0.9 to 1 for 10 different visible energy bins. Neutrino-electron elastic scattering events are shown as the hatched region in the "Others" category.

Fig. 16 shows the number of data and background events as a function of $\cos\theta$ for $\cos\theta > 0.9$, where neutrino-electron elastic scattering events are shown as the hatched region in the "Others" category and contribute to the $\cos\theta > 0.98$ bins. The neutrino-

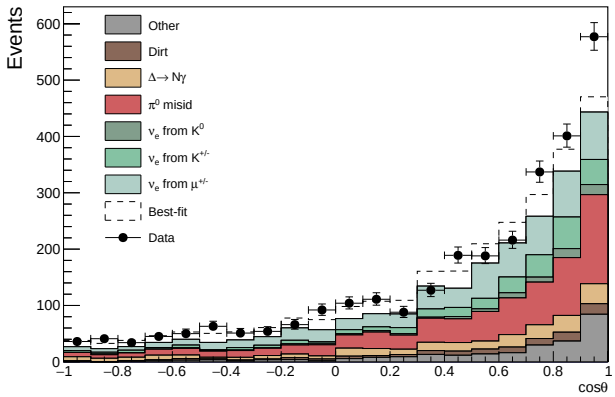

FIG. 8: The MiniBooNE neutrino mode $\cos\theta$ distributions, corresponding to the total 18.75×10^{20} POT data in the $200 < E_\nu^{QE} < 1250$ MeV energy range, for ν_e CCQE data (points with statistical errors) and background (colored histogram). The dashed histogram shows the best fit to the neutrino-mode data assuming two-neutrino oscillations.

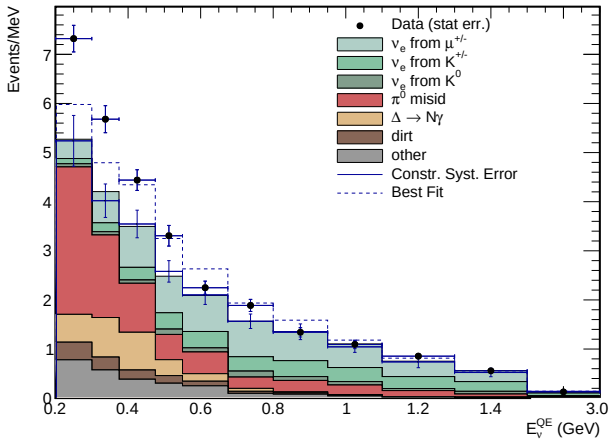

FIG. 9: The MiniBooNE neutrino mode E_ν^{QE} distributions, corresponding to the total 18.75×10^{20} POT data in the $200 < E_\nu^{QE} < 3000$ MeV energy range, for ν_e CCQE data (points with statistical errors) and predicted backgrounds (colored histograms). The constrained background is shown as additional points with systematic error bars. The dashed histogram shows the best fit to the neutrino-mode data assuming two-neutrino oscillations. The last bin is for the energy interval from 1500-3000 MeV.

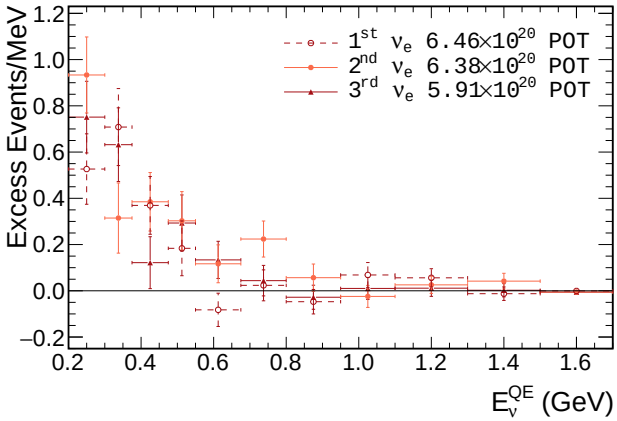

FIG. 10: The total event excesses in neutrino mode as a function of E_ν^{QE} for the first, second, and third running periods. Error bars include only statistical uncertainties.

TABLE III: *The fractional unconstrained systematic uncertainties in the* $200 < E_\nu^{QE} < 1250$ *MeV energy range.*

Systematic Uncertainty	Fraction of Event Excess
Cross Section	35%
Optical Model	23%
π^+ Production	14%
Neutrino Flux	7%
K^0 Production	4%
K^+ Production	4%

electron elastic events constitute 53% (89%) of the "Others" category for $\cos\theta > 0.90$ ($\cos\theta > 0.99$), and the category also includes neutrino-nucleon charged-current and neutral-current scattering events. As shown in the figure, the excess of data events over background events is approximately the same in each bin.

Figs. 17 and 18 show the E_ν^{QE} and $\cos\theta$ distributions for the $150 < E_\nu^{QE} < 1250$ MeV energy range, and the total event excess as a function of E_ν^{QE} is shown in Fig. 19. The solid curve on the latter plot shows the two-neutrino oscillation prediction at the best-fit point ($\sin^2 2\theta = 0.807$, $\Delta m^2 = 0.043$ eV^2). The lowest energy data point has less acceptance than the other data points due to the requirement that the visible energy be greater than 140 MeV. Table II lists the number of data events, background events, excess events, and excess

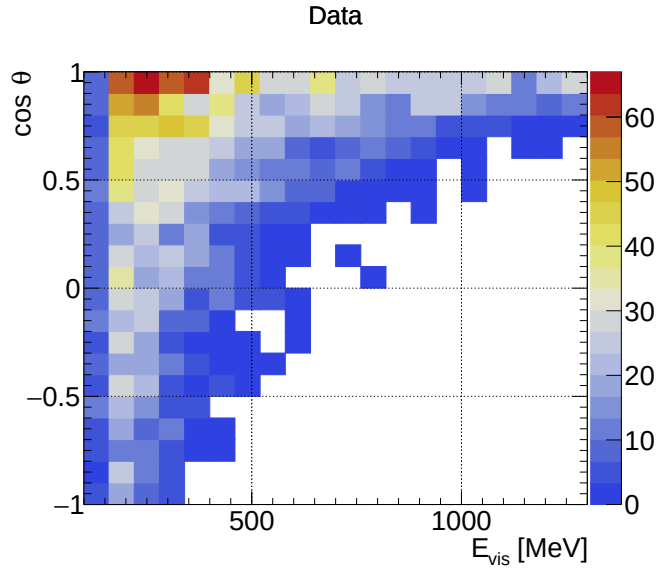

FIG. 11: The total numbers of data events in neutrino mode as functions of reconstructed visible energy and $\cos\theta$. There are 20 columns of visible energy from 150 to 1250 MeV and 20 rows of $\cos\theta$ from -1 to 1.

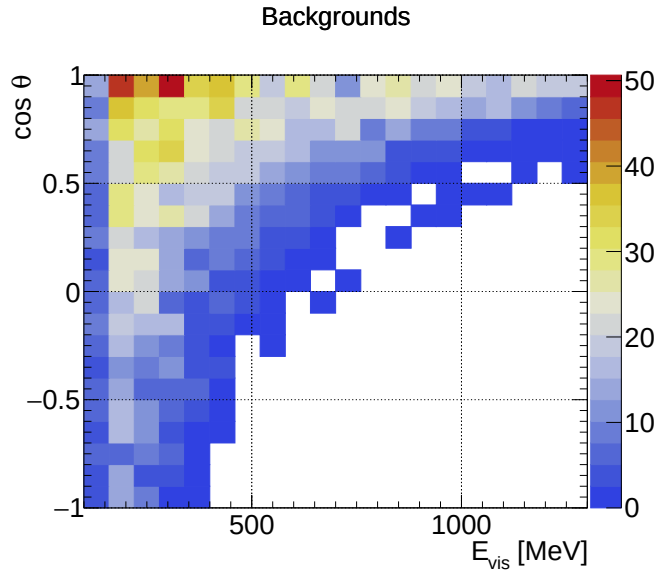

FIG. 12: The total numbers of background events in neutrino mode as functions of reconstructed visible energy and $\cos\theta$. There are 20 columns of visible energy from 150 to 1250 MeV and 20 rows of $\cos\theta$ from -1 to 1.

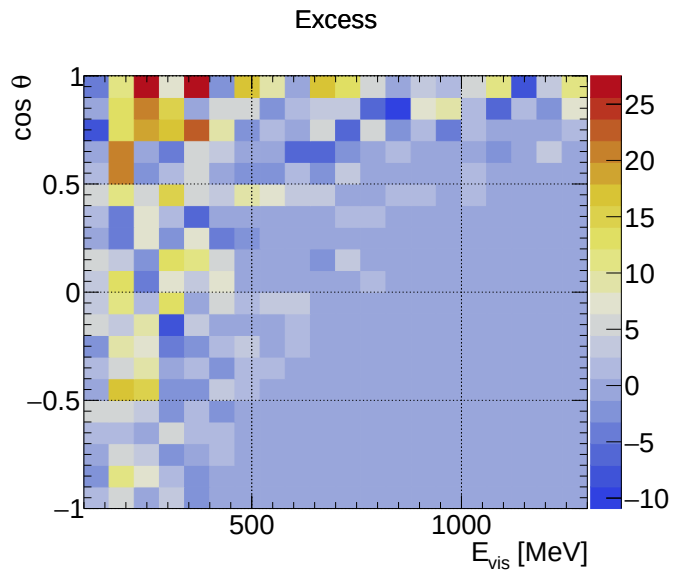

FIG. 13: The total numbers of excess events in neutrino mode as functions of reconstructed visible energy and $\cos\theta$. There are 20 columns of visible energy from 150 to 1250 MeV and 20 rows of $\cos\theta$ from -1 to 1.

significance for the $150 < E_\nu^{QE} < 1250$ MeV energy range.

V. NEUTRINO OSCILLATION FITS

Fig. 20 shows the MiniBooNE allowed regions in both neutrino mode and antineutrino mode [3] for events with $200 < E_\nu^{QE} < 3000$ MeV within a two-neutrino oscillation model. For this oscillation fit the entire data set is used and includes the 18.75×10^{20} POT data in neutrino mode and the 11.27×10^{20} POT data in antineutrino mode. Also shown are 90% C.L. limits from the KARMEN [26] and OPERA [27] experiments. The best combined neutrino oscillation fit occurs at $(\sin^2 2\theta,\ \Delta m^2) = (0.807,\ 0.043\ \text{eV}^2)$. The χ^2/ndf for the best-fit point in the energy range $200 < E_\nu^{QE} < 1250$ MeV is 21.7/15.5 with a probability of 12.3%, and the background-only fit has a χ^2 probability of 3×10^{-7} relative to the best oscillation fit and a $\chi^2/ndf = 50.7/17.3$ with a probability of 0.01%.

Fig. 21 compares the L/E_ν^{QE} distributions for the MiniBooNE data excesses in neutrino mode and antineutrino mode to the L/E distribution from LSND [1]. The error bars show statistical uncertainties only. As shown in the figure, there is agreement among all three data sets. Assuming two-neutrino oscillations, the curves show fits to the MiniBooNE data

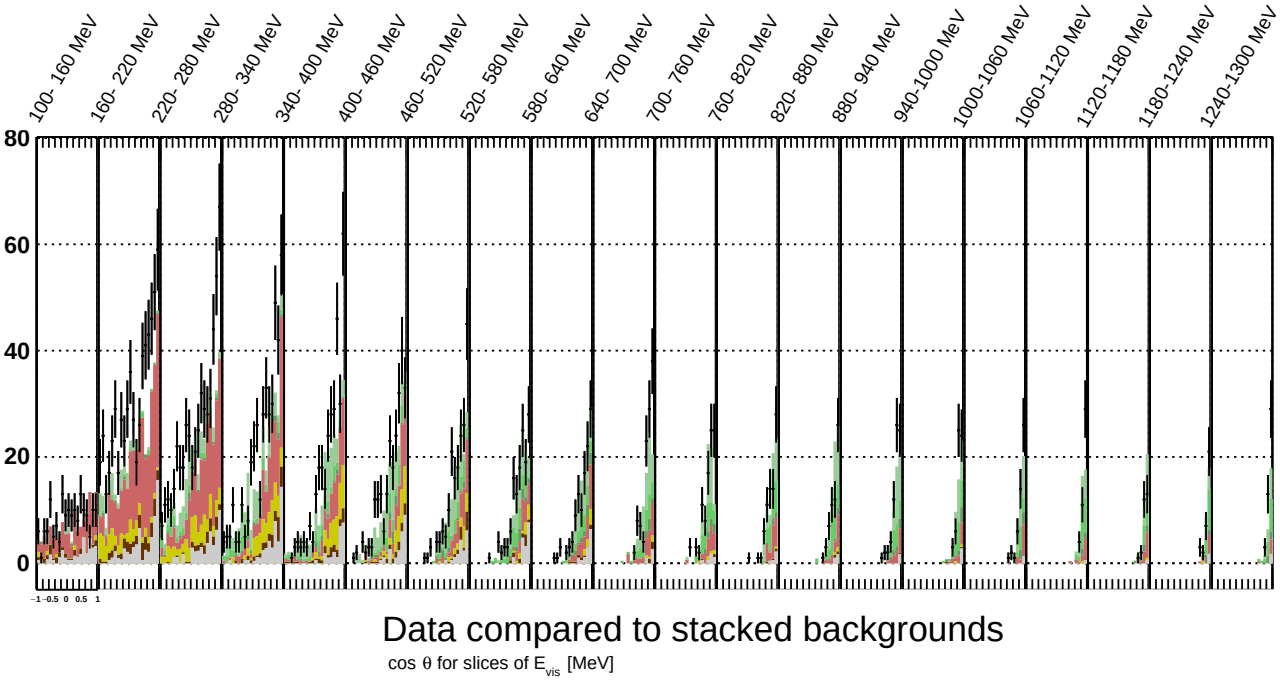

FIG. 14: The $\cos\theta$ distribution of data events (points with error bars) and background events (colored histogram) in neutrino mode for the 20 different visible energy bins from 150 to 1250 MeV.

described above. The significance of the combined LSND (3.8σ) [1] and MiniBooNE (4.8σ) excesses is 6.1σ, which is obtained by adding the significances in quadrature, as the two experiments have completely different neutrino energies, neutrino fluxes, reconstructions, backgrounds, and systematic uncertainties.

VI. BACKGROUND STUDIES AND CONSTRAINTS

Constraints have been placed on the various backgrounds in Table I by direct measurements of these backgrounds in the MiniBooNE detector. The ν_μ CC background has been well measured [28] by using the Michel electrons from muon decay to identify the event topology. Likewise, the NC π^0 background has also been well measured [29] by reconstructing the two-gamma invariant mass.

In addition, a fit to the vertex radial distribution, shown in Fig. 22, allows a constraint to be placed on the NC π^0 background, due to this background having more events near the

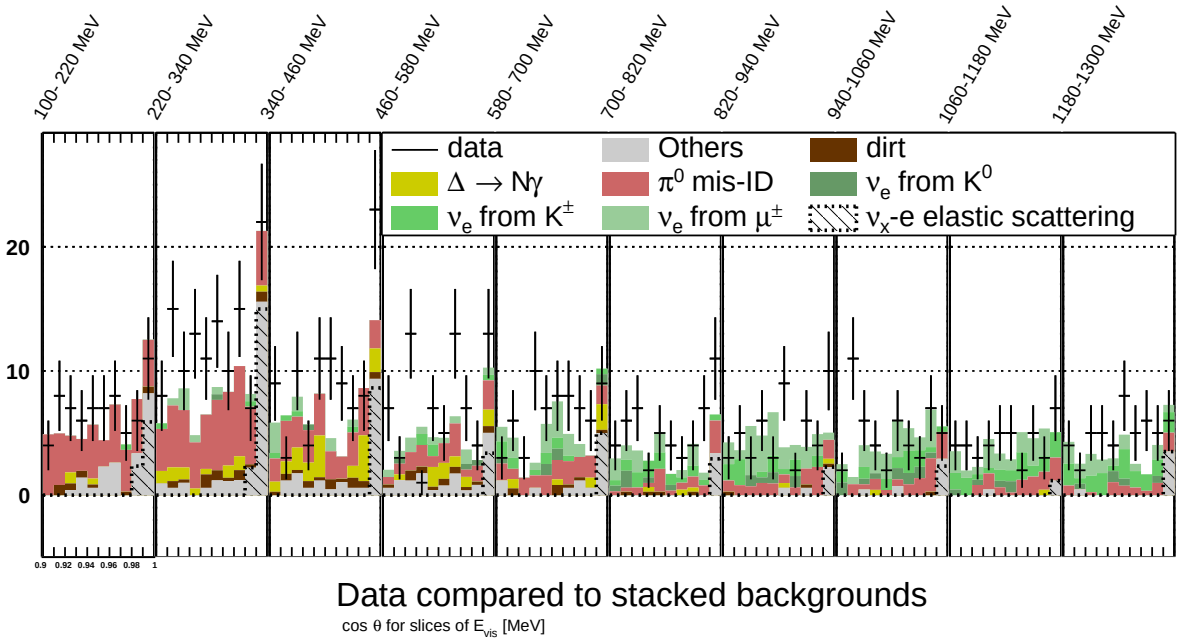

FIG. 15: The $\cos\theta$ distributions from 0.9 to 1 of data events (points with statistical errors) and background events (histogram) in neutrino mode for 10 different visible energy bins from 150 to 1250 MeV. Neutrino-electron elastic scattering events are shown as the hatched region in the "Others" category.

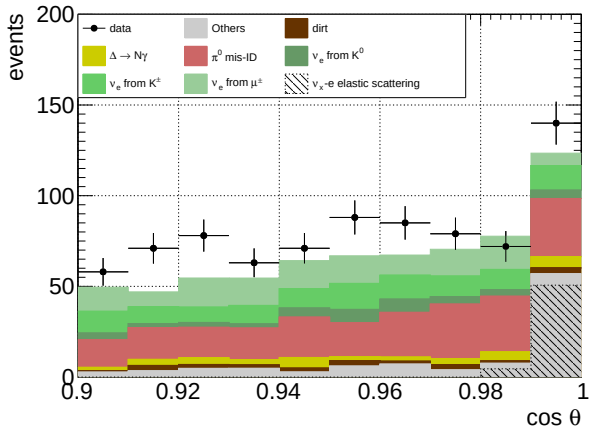

FIG. 16: The MiniBooNE neutrino mode $\cos\theta$ distribution for $\cos\theta > 0.9$, corresponding to the total 18.75×10^{20} POT neutrino data in the visible energy range from 150 to 1250 MeV, for ν_e CCQE data (points with statistical errors) and predicted backgrounds (colored histograms). Neutrino-electron elastic scattering events are shown as the hatched region in the "Others" category.

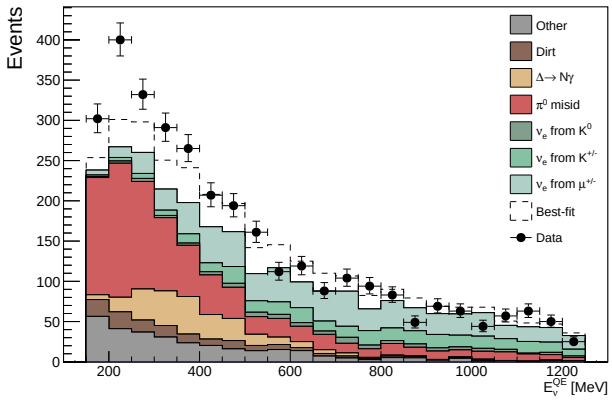

FIG. 17: The MiniBooNE neutrino mode E_ν^{QE} distributions, corresponding to the total 18.75×10^{20} POT neutrino data in the $150 < E_\nu^{QE} < 1250$ MeV energy range, for ν_e CCQE data (points with statistical errors) and predicted backgrounds (colored histograms). The dashed histogram shows the best fit to the neutrino-mode data assuming two-neutrino oscillations.

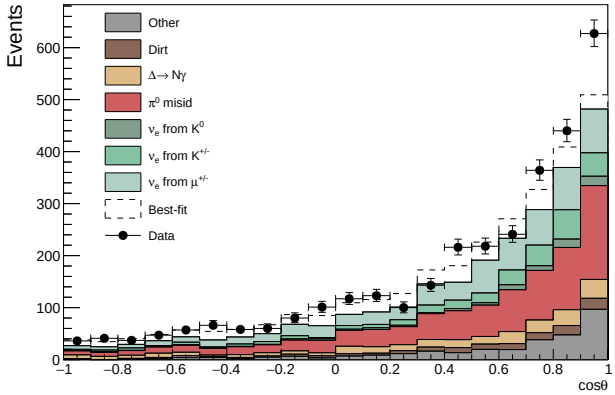

FIG. 18: The MiniBooNE neutrino mode $\cos\theta$ distributions, corresponding to the total 18.75×10^{20} POT neutrino data in the $150 < E_\nu^{QE} < 1250$ MeV energy range, for ν_e CCQE data (points with statistical errors) and predicted backgrounds (colored histograms). The dashed histogram shows the best fit to the neutrino-mode data assuming two-neutrino oscillations.

edge of the 5 m radius fiducial volume. (NC π^0 events near the edge of the fiducial volume have a greater chance of one photon leaving the detector with the remaining photon then misreconstructing as an electron candidate.) Fig. 23 shows the excess event radial distributions, where different processes are normalized to explain the event excess, while Table IV shows the result of log-likelihood shape-only fits to the radial distribution and the multiplicative

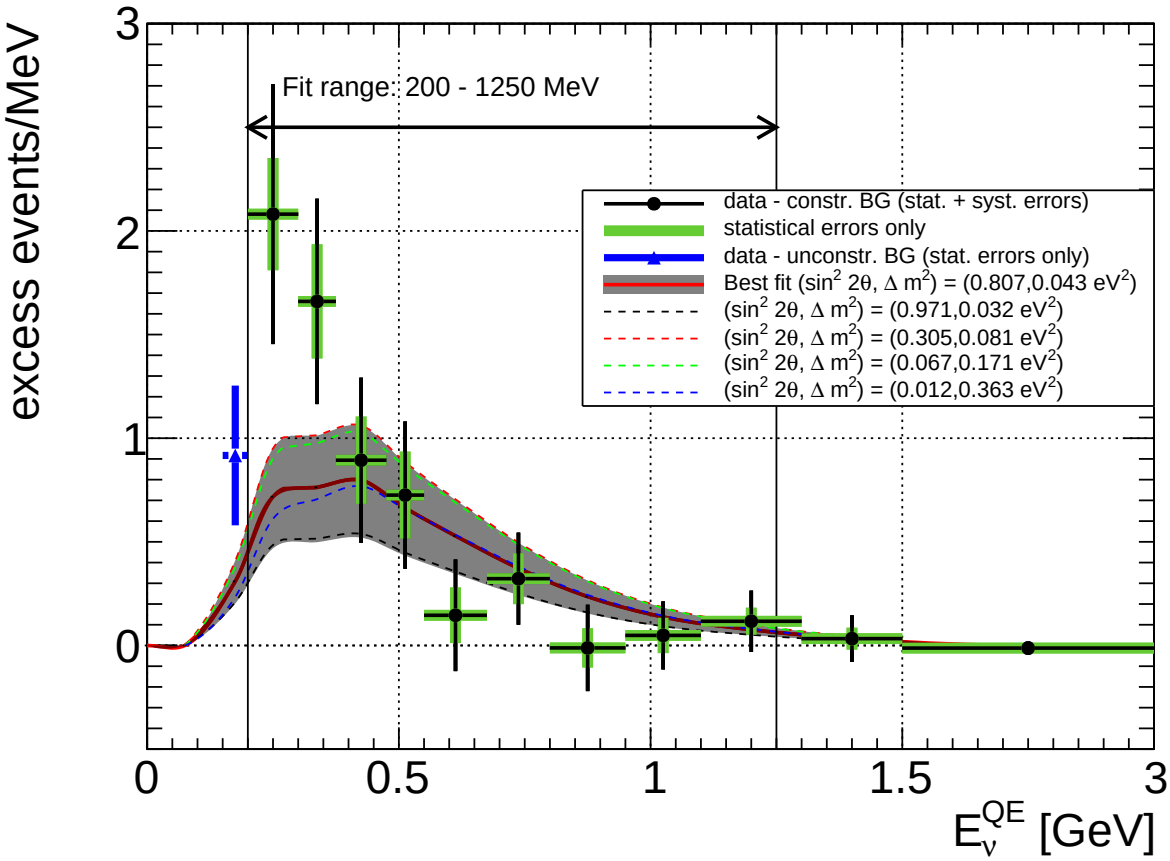

FIG. 19: The total event excess in neutrino mode, corresponding to 18.75×10^{20} POT in the $150 < E_\nu^{QE} < 3000$ MeV energy range. The solid curve shows the best fit to the neutrino-mode and antineutrino-mode data in the $200 < E_\nu^{QE} < 1250$ MeV energy range assuming two-neutrino oscillations, while the dashed curves show selected points on the 1 sigma contour. Also shown is the 1-sigma allowed band. The outer error bars include statistical plus constrained systematic uncertainties, while the inner error bars show the statistical uncertainties. The lowest energy data point shows only the unconstrained background statistical uncertainty.

factor that is required for each hypothesis to explain the observed event excess. The two-neutrino oscillation hypothesis fits the radial distribution best with a $\chi^2 = 8.4/9ndf$, while the NC π^0 hypothesis has a worse fit with a $\chi^2 = 17.2/9ndf$. The intrinsic ν_e backgrounds have a worse χ^2 than the two-neutrino oscillation hypothesis due to higher energy ν_e events having a different radial distribution than lower energy ν_e events.

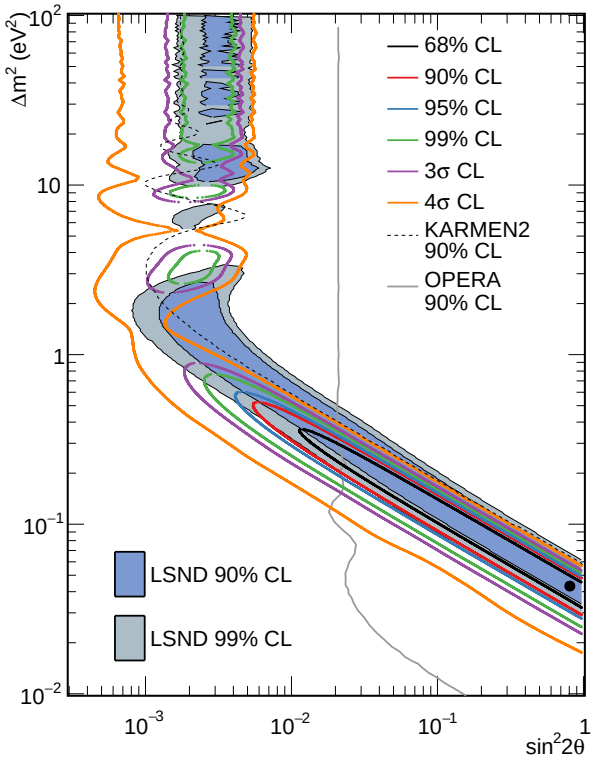

FIG. 20: MiniBooNE allowed regions for combined neutrino mode (18.75×10^{20} POT) and antineutrino mode (11.27×10^{20} POT) data sets for events with $200 < E_{\nu}^{QE} < 3000$ MeV within a two-neutrino oscillation model. The shaded areas show the 90% and 99% C.L. LSND $\bar{\nu}_{\mu} \rightarrow \bar{\nu}_{e}$ allowed regions. The black point shows the MiniBooNE best fit point. Also shown are 90% C.L. limits from the KARMEN [26] and OPERA [27] experiments.

Single-gamma backgrounds from external neutrino interactions ("dirt" backgrounds) are estimated using topological and spatial cuts to isolate the events whose vertices are near the edge of the detector and point towards the detector center [30]. The external event background estimate has been confirmed by measuring the absolute time of signal events relative to the proton beam microstructure (52.81 MHz extraction frequency), which corresponds to buckets of beam approximately every 18.9 ns. Fig. 24 shows that the event excess peaks in the 8 ns window associated with beam bunch time, as expected from neutrino events in the detector, and is inconsistent with external neutrino events or beam-off events, which would be approximately flat in time. Also, the observed background level outside of the beam agrees well with the predicted background estimate. In addition, good agreement is obtained for the event excess with $\cos\theta > 0.9$. The timing reconstruction performed here is

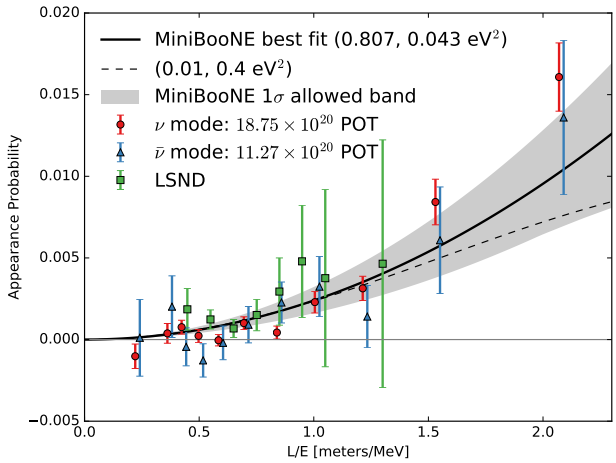

FIG. 21: A comparison between the L/E_ν^{QE} distributions for the MiniBooNE data excesses in neutrino mode (18.75×10^{20} POT) and antineutrino mode (11.27×10^{20} POT) to the L/E distribution from LSND [1]. The error bars show statistical uncertainties only. The curves show fits to the MiniBooNE data, assuming two-neutrino oscillations, while the shaded area is the MiniBooNE 1σ allowed band. The best-fit curve corresponds to $(\sin^2 2\theta,\ \Delta m^2) = (0.807,\ 0.043\ \text{eV}^2)$, while the dashed curve corresponds to a 1σ fit point at $(\sin^2 2\theta,\ \Delta m^2) = (0.01,\ 0.4\ \text{eV}^2)$.

similar to the reconstruction in reference [24], but with a different time offset applied.

The $\Delta \to N + \gamma$ background is determined from the NC π^0 event sample [29], which has contributions from Δ production in ^{12}C (52.2%), Δ production in H_2 (15.1%), coherent scattering on ^{12}C (12.5%), coherent scattering on H_2 (3.1%), higher-mass resonances (12.9%), and non-resonant background (4.2%). The fraction of Δ decays to π^0 is 2/3 from the Clebsch-Gordon coefficients, and the probability of pion escape from the ^{12}C nucleus is estimated to be 62.5%. The Δ radiative branching fraction is 0.60% for ^{12}C and 0.68% for H_2 after integration over all the invariant mass range, where the single gamma production branching ratio increases below the pion production threshold. With these values, the ratio of single gamma events to NC π^0 events, R, can be estimated to be

$$R = 0.151 \times 0.0068 \times 1.5 + 0.522 \times 0.0060 \times 1.5/0.625 = 0.0091.$$

Note that single gamma events are assumed to come entirely from Δ radiative decay. The total uncertainty on this ratio is 14.0% (15.6%) in neutrino (antineutrino) mode. This estimate of $R = 0.0091 \pm 0.0013$ agrees fairly well with theoretical calculations of the single gamma event rate [31].

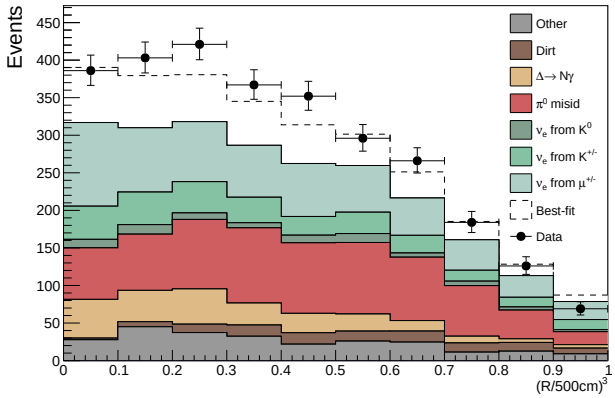

FIG. 22: The MiniBooNE radial vertex distribution, corresponding to the total 18.75×10^{20} POT data in neutrino mode in the $200 < E_\nu^{QE} < 1250$ MeV energy range, for ν_e CCQE data (points with statistical errors) and background (histogram). The dashed histogram shows the best fit to the neutrino-mode data assuming two-neutrino oscillations.

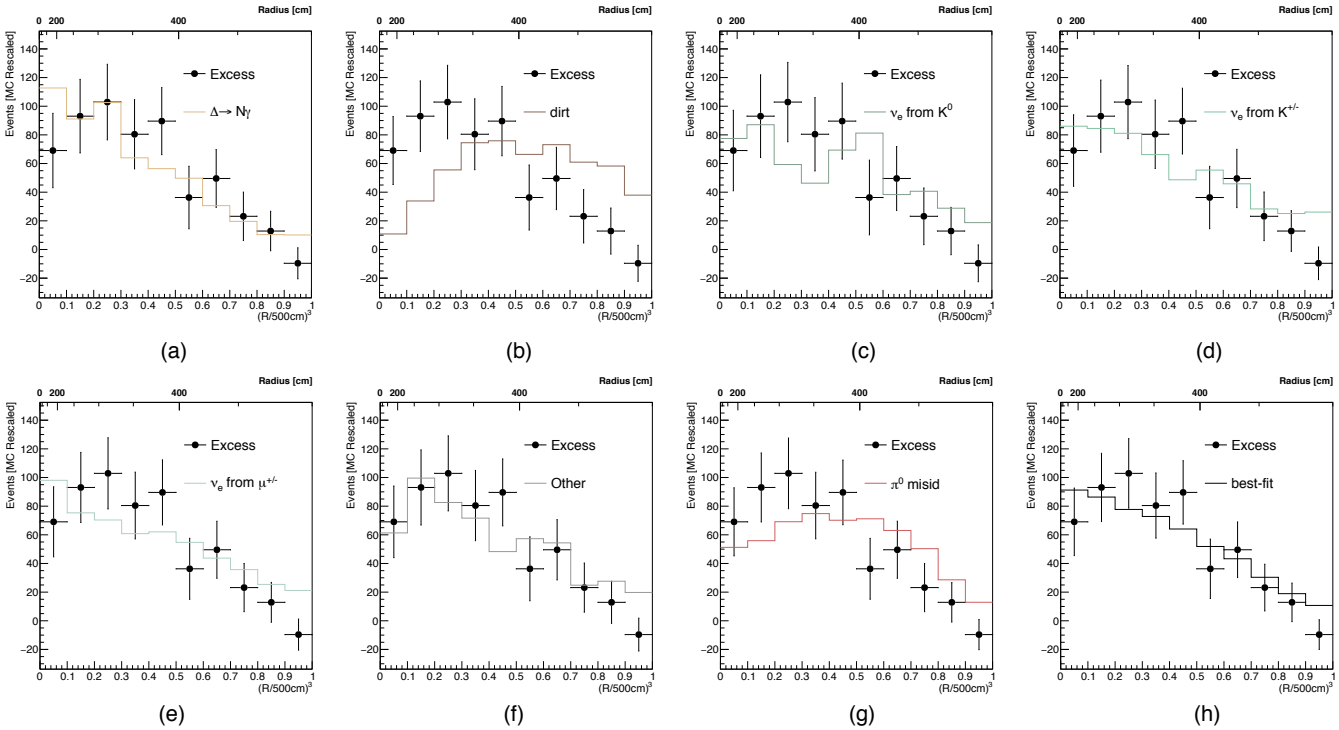

FIG. 23: The excess event radial distributions in neutrino mode with only statistical errors in the $200 < E_\nu^{QE} < 1250$ MeV energy range, where different processes are normalized to explain the event excess. The different processes are the following: (a) $\Delta \to N\gamma$; (b) External Events; (c) ν_e & $\bar{\nu}_e$ from K_L^0 Decay; (d) ν_e & $\bar{\nu}_e$ from $K^\pm$ Decay; (e) ν_e & $\bar{\nu}_e$ from $\mu^\pm$ Decay; (f) Other ν_e & $\bar{\nu}_e$; (g) NC π^0; (h) Best Fit oscillations.

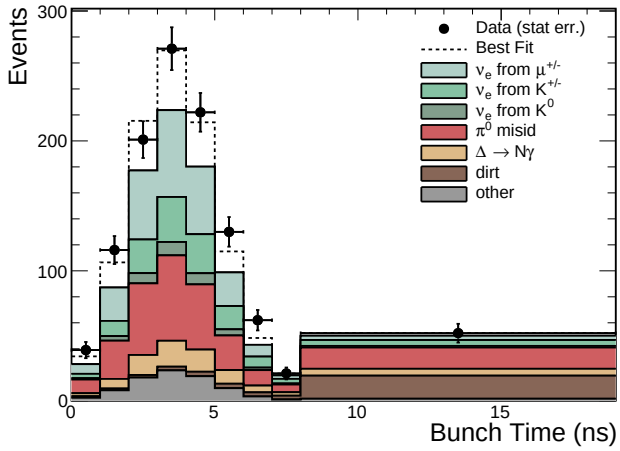

FIG. 24: The bunch timing for data events in neutrino mode compared to the expected background in the $200 < E_\nu^{QE} < 1250$ MeV energy range. Almost all of the excess data events occur, as expected from neutrino events in the detector, within the first 8 ns of the bunch timing. This data sample uses events collected with the new fiber timing system and represents about 40% of the entire neutrino mode sample.

The intrinsic ν_e background comes almost entirely from muon and kaon decay-in-flight in the beam decay pipe. MiniBooNE ν_μ CCQE event measurements [28] constrain the size and energy dependence of the intrinsic ν_e background from muon decay, while the intrinsic ν_e background from kaon decay is constrained by fits to kaon production data and SciBooNE measurements [32]. Furthermore, due to the higher energy of the intrinsic ν_e background, this background is disfavored from the fit to the radial distribution, as shown in Table IV.

Finally, backgrounds from exotic π^0 decay in the neutrino production target are ruled out from the MiniBooNE beam-dump run, where the incident proton beam was steered above the Be target and interacted in the steel beam dump at the downstream end of the decay pipe. No excess of events was observed [24], which set limits on light dark matter and other exotic π^0 decays.

VII. CONSTRAINTS ON NC π^0 BACKGROUND WITH TIGHTER RADIUS SELECTION

Explanations for the event excess have included unsimulated photons entering the detector from external interactions and the undersimulation of photons lost from π^0 production within the detector. To test these explanations in a model-independent way, we can use

TABLE IV: *The result of log-likelihood shape-only fits to the radial distribution in neutrino mode, assuming only statistical errors, where different processes are normalized to explain the observed event excess. The two-neutrino hypothesis fits the radial distribution best with a* $\chi^2 = 8.4/9ndf$*, while the NC* π^0 *hypothesis has a worse fit with a* $\chi^2 = 17.2/9ndf$*. Also shown is the multiplicative factor that is required for each hypothesis to explain the observed event excess.*

Hypothesis	Multiplicative factor	$\chi^2/9ndf$
NC $\Delta \to N\gamma$ Background	3.18	10.0
External Event Background	5.98	44.9
ν_e & $\bar{\nu}_e$ from K_L^0 Decay Background	7.85	14.8
ν_e & $\bar{\nu}_e$ from $K^\pm$ Decay Background	2.95	16.3
ν_e & $\bar{\nu}_e$ from $\mu^\pm$ Decay Background	1.88	16.1
Other ν_e & $\bar{\nu}_e$ Background	3.21	12.5
NC π^0 Background	1.75	17.2
Best Fit Oscillations	1.24	8.4

our higher event statistics to study the change in the excess as a function of tighter fiducial volume cuts. The NC π^0 and external event backgrounds preferentially populate higher radius compared to electron neutrino interactions. Therefore, reducing the fiducial radius is expected to reduce the significance of the excess if it is due to these backgrounds and increase the significance of the excess if its distribution is ν_e-like. If we change the standard 5 m cut to 4 m, we find there are 1978 data events in neutrino mode, 1519.4 ± 81.9 background events, and an excess of 458.6 ± 81.9 events (5.6σ). If we use a 3 m cut, we find 864 data events, 673.9 ± 41.2 background events, and an excess of 190.1 ± 41.2 events (4.6σ), consistent with what is expected if the signal is more ν_e-like. The event statistics are shown in Table II, while Figs. 25 and 26 show the reconstructed neutrino energy and $\cos\theta$ distributions for electronlike events with radius less than 4 m for both data events and background events.

VIII. CONCLUSION

In summary, the MiniBooNE experiment observes a total excess of $638.0 \pm 52.1(stat.) \pm 132.8(syst.)$ electronlike events in the energy range $200 < E_\nu^{QE} < 1250$ MeV in both neutrino

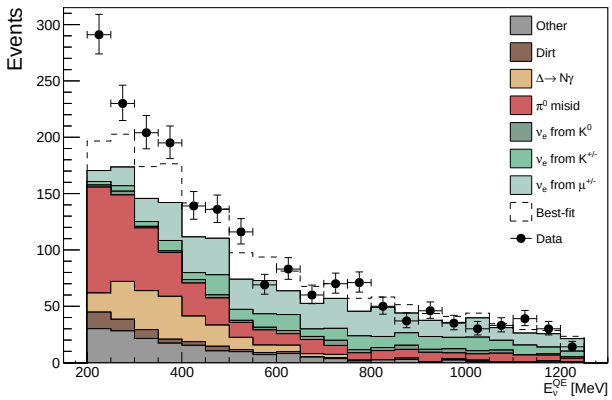

FIG. 25: The MiniBooNE neutrino mode E_ν^{QE} distributions, corresponding to the total 18.75×10^{20} POT data in neutrino mode in the $200 < E_\nu^{QE} < 1250$ MeV energy range, for ν_e CCQE data (points with statistical errors) and background (histogram) with radius less than 4 m. The dashed histogram shows the best fit to the neutrino-mode data assuming two-neutrino oscillations.

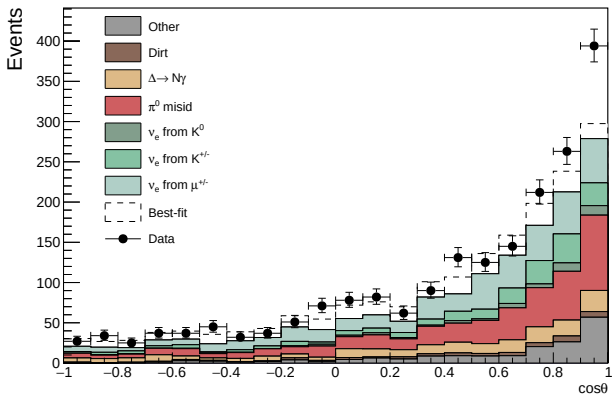

FIG. 26: The MiniBooNE neutrino mode $\cos\theta$ distributions, corresponding to the total 18.75×10^{20} POT data in neutrino mode in the $200 < E_\nu^{QE} < 1250$ MeV energy range, for ν_e CCQE data (points with statistical errors) and background (histogram) with radius less than 4 m. The dashed histogram shows the best fit to the neutrino-mode data assuming two-neutrino oscillations.

and antineutrino running modes. The overall significance of the excess, 4.8σ, is limited by systematic uncertainties, assumed to be Gaussian, as the statistical significance of the excess is 12.2σ. All of the major backgrounds are constrained by in situ event measurements. Beam timing information shows that almost all of the excess is in time with neutrinos that interact in the detector. The radius distribution shows that the excess is distributed throughout the volume, while tighter cuts on the fiducal volume increase the significance of the excess. The data likelihood ratio disfavors models that explain the event excess due to entering or exiting photons. The MiniBooNE event excess will be further studied by the Fermilab short-baseline

neutrino (SBN) program [33] and by the JSNS^2 experiment at J-PARC [34].

Acknowledgments

We acknowledge the support of Fermilab, the Department of Energy, and the National Science Foundation, and we acknowledge Los Alamos National Laboratory for LDRD funding.

---

[1] C. Athanassopoulos *et al.*, Phys. Rev. Lett. 75, 2650 (1995); 77, 3082 (1996); 81, 1774 (1998); Phys. Rev. C. **54**, 2685 (1996); **58**, 2489 (1998); A. Aguilar *et al.*, Phys. Rev. D 64, 112007 (2001).

[2] A. A. Aguilar-Arevalo *et al.*, Phys. Rev. Lett. 98, 231801 (2007); Phys. Rev. Lett. 102, 101802 (2009); Phys. Rev. Lett. 105, 181801 (2010); Phys. Rev. Lett. 110, 161801 (2013).

[3] A. A. Aguilar-Arevalo *et al.*, Phys. Rev. Lett. 121, 221801 (2018).

[4] M. Sorel, J. M. Conrad, and M. H. Shaevitz, Phys. Rev. D 70, 073004 (2004).

[5] G. Karagiorgi, Z. Djurcic, J. M. Conrad, M. H. Shaevitz, and M. Sorel, Phys. Rev. D 80, 073001 (2009); D 81, 039902(E) (2010).

[6] G.H. Collin, C.A. Argüelles, J.M. Conrad, and M.H. Shaevitz, Phys. Rev. Lett. 117, 221801 (2016).

[7] C. Giunti and M. Laveder, Phys. Lett. B 706, 200 (2011); Phys. Rev. D84, 073008, (2011).

[8] S. Gariazzo, C. Giunti, M. Laveder, and Y.F. Li, J. High Energy Phys. 06 (2017) 135.

[9] Sebastian Boser, Christian Buck, Carlo Giunti, Julien Lesgourgues, Livia Ludhova, Susanne Mertens, Anne Schukraft, and Michael Wurm, Prog. Part. Nucl. Phys. 111 (2020) 103736.

[10] J. Kopp, M. Maltoni, and T. Schwetz, Phys. Rev. Lett. 107, 091801 (2011); Joachim Kopp, Pedro A.N. Machado, Michele Maltoni, and Thomas Schwetz, J. High Energy Phys. 05 (2013) 050.

[11] Mona Dentler, Alvaro Hernandez-Cabezudo, Joachim Kopp, Pedro Machado, Michele Maltoni, Ivan Martinez-Soler, and Thomas Schwetz, J. High Energy Phys. 08 (2018) 010.

[12] K. N. Abazajian et al., arXiv:1204.5379.

[13] J. M. Conrad, C. M. Ignarra, G. Karagiorgi, M. H. Shaevitz, and J. Spitz, Adv. High Energy Phys. 2013, 1 (2013).

[14] A. Diaz, C. A. Argüelles, G. H. Collin, J. M. Conrad, and M. H. Shaevitz, Phys. Rep. 884, 1 (2020).

[15] J. Asaadi, E. Church, R. Guenette, B. J. P. Jones, and A. M. Szelc, Phys. Rev. D 97, 075021 (2018); G. Karagiorgi, M. H. Shaevitz, and J. M. Conrad, arXiv:1202.1024; Heinrich Paes, Sandip Pakvasa, and Thomas J. Weiler, Phys. Rev. D 72, 095017 (2005); Dominik Doring, Heinrich Pas, Philipp Sicking, and Thomas J. Weiler, Eur. Phys. J. C 80, 1202 (2020).

[16] V. A. Kostelecky and M. Mewes, Phys. Rev. D 69, 016005 (2004); T. Katori, V. A. Kostelecky, and R. Tayloe, Phys. Rev. D 74, 105009 (2006); Jorge S. Diaz and V. A. Kostelecky, Phys. Lett. B 700, 25 (2011); Jorge S. Diaz and V. A. Kostelecky, Phys. Rev. D 85, 016013 (2012).

[17] S. N. Gninenko, Phys. Rev. Lett. 103, 241802 (2009); S. N. Gninenko and D. S. Gorbunov, Phys. Rev. D 81, 075013 (2010); Yang Bai, Ran Lu, Sida Lu, Jordi Salvado, and Ben A. Stefanek, Phys. Rev. D 93, 073004 (2016); Zander Moss, Marjon H. Moulai, Carlos A. Argüelles, and Janet M. Conrad, Phys. Rev. D 97, 055017 (2018); Enrico Bertuzzo, Sudip Jana, Pedro A. N. Machado, and Renata Zukanovich Funchal, Phys. Rev. Lett. 121, 241801 (2018); Peter Ballett, Silvia Pascoli, and Mark Ross-Lonergan, Phys. Rev. D 99, 071701 (2019); Oliver Fischer, Alvaro Hernandez-Cabezudo, and Thomas Schwetz, Phys. Rev. D 101 7, 075045 (2020); M. H. Moulai, C. A. Argüelles, G. H. Collin, J. M. Conrad, A. Diaz, and M. H. Shaevitz, Phys. Rev. D 101, 055020 (2020); Mona Dentler, Ivan Esteban, Joachim Kopp, and Pedro Machado, Phys. Rev. D 101, 115013 (2020); Andre de Gouvea, O. L. G. Peres, Suprabh Prakash, and G. V. Stenico, JHEP 07, 141 (2020); Carlos A. Argüelles, Matheus Hostert, and Yu-Dai Tsai, Phys. Rev. Lett. 123, 261801 (2019); Alakabha Datta, Saeed Kamali, and Danny Marfatia, Phys. Lett. B 807, 135579 (2020); Asli Abdullahi, Matheus Hostert, and Silvia Pascoli, arXiv:2007.11813.

[18] Bhaskar Dutta, Sumit Ghosh, and Tianjun Li, Phys. Rev. D 102, 055017 (2020); Waleed Abdallah, Raj Gandhi, and Samiran Roy, JHEP 12, 188 (2020); Waleed Abdallah, Raj Gandhi, and Samiran Roy, arXiv:2010.06159.

[19] Jiajun Liao and Danny Marfatia, Phys. Rev. Lett. 117, 071802 (2016).

[20] Marcela Carena, Ying-Ying Li, Camila S. Machado, Pedro A. N. Machado, Carlos E. M. Wagner, Phys. Rev. D 96, 095014 (2017).

[21] A. A. Aguilar-Arevalo *et al.*, Nucl. Instrum. Methods Phys. Res., Sect. A 599, 28 (2009).

[22] R. B. Patterson, E. M. Laird, Y. Liu, P. D. Meyers, I. Stancu, and H. A. Tanaka, Nucl. Instrum. Methods Phys. Res., Sect. A 608, 206 (2009).

[23] A. A. Aguilar-Arevalo *et al.*, Phys. Rev. D 81, 092005 (2010); A. A. Aguilar-Arevalo *et al.*, Phys. Rev. D 88, 032001 (2013).

[24] A. A. Aguilar-Arevalo *et al.* (MiniBooNE Collaboration), Phys. Rev. Lett. **118**, 221803 (2017); A. A. Aguilar-Arevalo *et al.* (MiniBooNE Collaboration), Phys. Rev. D 98, 112004 (2018).

[25] A. A. Aguilar-Arevalo *et al.*, Phys. Rev. D 84, 072005 (2011).

[26] B. Armbruster *et al.*, Phys. Rev. D 65, 112001 (2002).

[27] N. Agafonova *et al.*, arXiv:1803.11400.

[28] A. A. Aguilar-Arevalo *et al.*, Phys. Rev. D 81, 092005 (2010); Phys. Rev. Lett. 100, 032301 (2008).

[29] A. A. Aguilar-Arevalo *et al.*, Phys. Rev. D 81, 013005 (2010); Phys. Lett. B. 664, 41 (2008).

[30] A. A. Aguilar-Arevalo *et al.*, Phys. Rev. Lett. 102, 101802 (2009).

[31] D. Rein and L. M. Sehgal, Phys. Lett. 104B, 394 (1981); S. S. Gershtein, Yu. Ya. Komachenko, and M. Yu. Khlopov, Sov. J. Nucl. Phys. 33, 860 (1981); Jeffrey A. Harvey, Christopher T. Hill, and Richard J. Hill, Phys. Rev. Lett. 99, 261601 (2007); Tina Leitner, Oliver Buss, Ulrich Mosel, and Luis Alvarez-Ruso, arXiv:0809.3986; J. P. Jenkins and T. Goldman, Phys. Rev. D 80, 053005 (2009); Artur M. Ankowski, Omar Benhar, Takaaki Mori, Ryuta Yamaguchi, and Makoto Sakuda, Phys. Rev. Lett. 108, 052505 (2012); K. M. Graczyk, D. Kielczewska, P. Przewlocki, and J. T. Sobczyk, Phys. Rev. D 80, 093001 (2009); V. P. Efrosinin, Yu. G. Kudenko, and A. N. Khotjantsev, Phys. At. Nucl. 72, 459 (2009); Richard J. Hill, Phys. Rev. D 81, 013008 (2010); Richard J. Hill, Phys. Rev. D 84, 017501 (2011); Xilin Zhang and Brian D. Serot, Phys. Lett. B 719, 409 (2013); Phys. Rev. C **86**, 035502 (2012); Phys. Rev. C **86**, 035504 (2012); Brian D. Serot and Xilin Zhang, Phys. Rev. C **86**, 015501 (2012); E. Wang, L. Alvarez-Ruso, and J. Nieves, Phys. Rev. C **89**, 015503 (2014); Phys. Lett. B 740, 16 (2015).

[32] G. Cheng *et al.*, Phys. Rev. D 84, 012009 (2011); C. Mariani, G. Cheng, J. M. Conrad and M. H. Shaevitz, Phys. Rev. D **84**, 114021 (2011).

[33] M. Antonello *et al.*, arXiv:1503.01520.

[34] M. Harada *et al.*, arXiv:1310.1437.